DOI: 10.13009/EUCASS2017-561

Numerical investigation of the turbulent wake of a generic space launcher at transonic speed

S. Loosen⋆†*, V. Statnikov*⋆*, M. Meinke*⋆,⋆⋆ *and W. Schröder*⋆,⋆⋆
⋆ *Institute of Aerodynamics and Chair of Fluid Mechanics*
RWTH Aachen University, Wüllnerstraße 5a, 52062 Aachen, Germany
⋆⋆ *Forschungszentrum Jülich, 52428 Jülich, JARA - High-Performance Computing*
e-mail: s.loosen@aia.rwth-aachen.de
†Corresponding author

Abstract

The turbulent wake of a generic planar space launcher configuration with an overexpanded jet is numerically investigated at transonic freestream conditions ($M_\infty = 0.8$ and $Re_D = 4.3 \cdot 10^5$) by a zonal Reynolds averaged Navier-Stokes/large-eddy simulation (RANS/LES) method and the dynamic mode decomposition (DMD) approach. Particular attention is paid on the influence of the overexpanded jet on the wake flow modes, which are responsible for the buffet phenomenon, by comparing the results to a previous investigation of a backward-facing step (BFS) configuration excluding the overexpanded jet. The jet suction effect causes a streamwise acceleration of the wake flow leading to an impingement of the shed shear layer on the nozzle further upstream and to a reduced base pressure. Using temporal Fourier transform and DMD, three stable modes at $Sr_{D,1} = 0.04$, $Sr_{D,2} = 0.14$, and $Sr_{D,3} = 0.23$ are extracted. The low frequency mode describes a periodical growth and shrinkage of the recirculation bubble and the two higher frequency modes reflect an undulating motion of the shear layer. The first and third mode are very similar to the "cross-pumping" and "cross-flapping" motion detected in the jetless BFS configuration. The second mode, however, was not found before. The finite length of the nozzle extension and the overexpanded jet seem to promote the formation and shedding of large-scale spanwise rotational structures causing a streamwise wave-like motion of the shear layer which is connected to the second mode.

1. Introduction

One of the challenging tasks for the design of more efficient launch vehicles is the understanding and control of low frequency wall pressure fluctuations leading to undesired structural vibrations known as the buffeting phenomenon. The outer geometry of the afterbody of a classical launcher's main stage is characterized by an abrupt change from the diameter of the rocket to that of the thrust nozzle causing the incoming turbulent boundary layer to separate at the base shoulder. As a first consequence of this separation, the base drag is substantially increased due to the low pressure level within the recirculation region compared to the freestream conditions. Furthermore, during the first phase of the launch trajectory up to an altitude of several kilometers, the highly unsteady shed shear layer impinges on the thrust nozzle just upstream of its end leading to substantial wall pressure fluctuations. The main flow structures are sketched in Fig. 1. As a result of the pressure fluctuations, so called low frequency buffet loads occur which can lead to the aforementioned buffeting phenomenon, if the frequency of the loads excites structural modes of the thrust nozzle. During the high dynamic pressure phase of the flight at a freestream Mach number of $M_\infty = 0.8$, the aerodynamic loads feature the highest amplitudes which can disturb the launchers stability or even result in critical structural damage leading to a complete loss of the launcher under unfavorable circumstances.

The turbulent wake flow behind the base of the rocket exhibits many similarities with separating-reattaching flows of blunt bodies extensively studied in the last decades. According to Deprés et al.[1] two types of base flow separation can be distinguished. The first type is characterized by a downstream reattachment of the separated shear layer on a solid surface, in the second no reattachment occurs. Since this study deals with the first type only, the following overview focuses on the former.

One of the simplest separating-reattaching flow is the flow past a planar backward-facing step (BFS) which is characterized by a straight and fixed separation line and features many similarities to the wake dynamic and shear layer instabilities of axisymmetric space launchers. This flow has been extensively studied experimentally, e.g., by Bradshaw

DOI: 10.13009/EUCASS2017-561

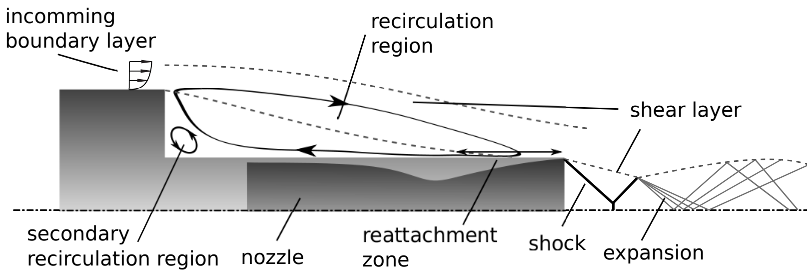

Figure 1: Schematic representation of the investigated wake topology including an overexpanded nozzle jet.

& Wong,[2] Eaton & Johnston,[3] Driver et al.,[4] and Simpson,[5] and numerically, e.g., by Friedrich & Arnal,[6] Silveira Neto et al.,[7] Le et al.,[8] and Lee & Sung.[9] In all these investigations a variation of the instantaneous impingement location of the separated shear layer by about two step heights around the mean reattachment position is reported. In addition, two basic modes of characteristic frequencies were detected in nearly all of these studies. The low frequency mode at a Strouhal number of $Sr_h = 0.012 - 0.014$ based on the step height and the freestream velocity reflects an overall increase and decrease of the separation bubble or shear-layer "flapping" as it is commonly called in the literature. The aforementioned time dependent variation of the instantaneous reattachment position can be attributed to this "flapping" motion. The first attempt to explain this "flapping" motion was given by Driver et al.[4] who attributed the shrinking size of the separation bubble to large vortical structures containing more forward momentum than its neighbors escaping the reattachment region without losing too much mass in the recirculation bubble. The higher frequency mode at $Sr_h = 0.065-0.08$ is attributed to a Kelvin-Helmholtz like vortex-shedding instability. The studies on planar BFS flows are mainly limited to two-dimensional observations or spanwise averaged flow properties. More recently, Statnikov et al.[10] and Scharnowski et al.[11] analyzed the three-dimensional wake of a generic planar launcher consisting of a BFS with a long forebody. It was shown that the reattachment position varies over time not only in the streamwise but also in the spanwise direction leading to a formation of wedge-shaped reattachment regions. Using a DMD analysis this variation in the reattachment process can be traced back to a coherent longitudinal cross-pumping motion of the recirculation bubble at $Sr_h = 0.012$ and a cross-flapping motion of the shear layer at $Sr_h = 0.07$.

Besides the presented studies on planar configurations many experimental and numerical investigations on a large range of different axisymmetric more realistic space launcher configurations ranging from axisymmetric backward-facing steps up to scaled real launchers including the solid booster have been conducted, e.g. Deprés et al.,[1] Deck & Thorigny,[12] Pain et al.,[13] Marié et al.,[14] Schrijer et al.,[15] and Statnikov et al.[16,17] . Schrijer et al. used proper orthogonal decomposition (POD) to analyze a time series of snapshots of 2D-PIV measurements and detected two dominant wake modes containing the majority of the turbulent kinetic energy. The first low frequency mode captures an oscillating growing and shrinking of the separation zone, most probably being the counterpart of the shear-layer "flapping" detected in the planar BFS flows or to the more recently observed three-dimensional cross-pumping motion by Statnikov et al.[10] in a planar space launcher configuration. The second higher frequency mode describes an undulating motion of the shear layer coinciding with the vortex-shedding of the BFS flow (Le et al.[8]) and the cross-flapping motion of the planar space launcher (Statnikov et al.[10]). Deprés et al.[1] and Deck & Thorigny[12] experimentally and numerically investigated the wake of an axisymmetric launcher configuration. Using two-point correlation analysis on the instantaneous wall pressure signal located at opposite sides in the azimuthal direction on the nozzle, an anti-phase oscillation at a Strouhal number of $Sr_D \approx 0.2$ was detected causing undesired side loads. They assumed that those periodic side loads are generated by helical vortical structures in the wake. Such a helical mode, however, has not been visualized yet. More recently, Statnikov et al.[10] performed a dynamic mode decomposition of the flow around a generic Ariane 5-like configuration to analyze the coherent structures being responsible for the side forces. Three distinct modes at $Sr_D \approx 0.1; 0.2; 0.35$ which could generate buffet were detected. The low frequency mode describes a longitudinal cross-pumping motion of the separation region, the second mode is associated with a cross-flapping motion of the shear layer caused by antisymmetric vortex shedding, and the high frequency mode represents a swinging motion of the shear layer.

The study is a continuation of the aforementioned investigation on the pressure fluctuations of a planar transonic backward-facing step configuration by Statnikov et al.[10] , where the effect of the overexpanded jet during the transonic trajectory stage was neglected. In the present investigation, a planar configuration with a thrust-optimized nozzle is used to take into account the effect of the overexpanded jet on the wake dynamic. The present work also serves as a reference case for an upcoming evaluation of advanced future propulsion concepts like the dual-bell nozzle which allows a one-step altitude adaption to changing freestream conditions during the flight trajectory. In these configurations, particular

DOI: 10.13009/EUCASS2017-561

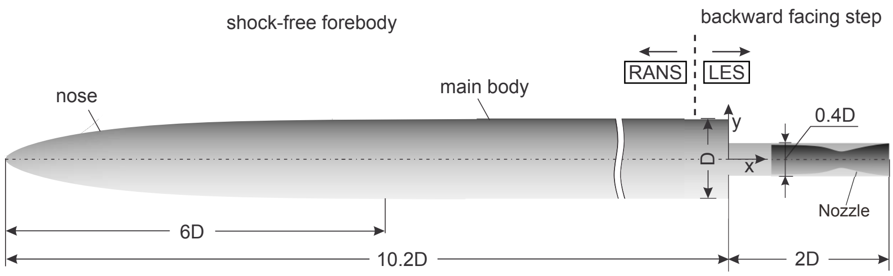

Figure 2: Geometry parameters of the investigated generic planar transonic configuration.

attention is paid to a possible coupling between the outer and inner separation during the sea-level mode leading to additional dynamic forces.

Besides classical statistical analyses such as mean and root-mean-square distributions and spectral analyses, the dynamic mode decomposition (DMD) approach is used to analyze the wake flow. The turbulent wake of the generic space launchers is characterized by a superposition of flow structures exhibiting various time and length scales. Therefore, it is a challenging task to identify those wake flow mechanisms which are responsible for distinct frequencies observed, e.g., in the pressure spectra. The DMD method, which belongs to a class of data-driven modal decomposition techniques, allows to isolate spatial modes of defined frequency in the wake flow such that insight into the underlying flow mechanisms is obtained. For instance, Statnikov et al.[10,17] successfully applied DMD to time-resolved numerical data of transonic and supersonic wake flows of generic space launchers to determine coherent multi-dimensional flow patterns. In the following, DMD is used to understand the underlying flow phenomena leading to the periodic behavior of the wake flow determined by classical spectral analysis.

The paper is organized as follows. In Sec. 2, the investigated geometry and the flow parameters are presented. The zonal RANS/LES method, the computational grids, and the DMD algorithm are briefly described. In Sec. 3, the results of the performed simulations are discussed. First, the wake flow topology with jet is described and compared to the pure jetless BFS configuration. Then, a spectral analysis of the wall pressure fluctuations is performed followed by a modal analysis of the wake flow by DMD. Finally, conclusions are drawn and an outlook is given in Sec. 4.

2. Computational Approach

In this section, the computational approach, i.e., the investigated geometry and flow parameters, the zonal RANS/LES method, the computational grids, and the DMD algorithm is disscussed.

2.1 Geometry and flow conditions

The influence of the overexpanded jet emanating from the nozzle on the transonic wake flow is investigated for a planar generic space launcher configuration, shown in Fig. 2. The setup is based on the geometry in [10] , where the effect of the nozzle was not considered. The launcher model, which was defined in the framework of the German Collaborative Research Center Transregio 40 [10] , is composed of a main body with a reference thickness of D and a length of $4.2\,D$ and a long shock-free nose with a length of 6D to avoid an undesired shock-boundary interaction upstream of the investigated wake flow. Note that compared to the setup used in Statnikov et al.[10] the length of the main body is increased by $0.2\,D$. To model the tail of the launcher including the engine, an extension with a thickness of $0.4\,D$ and a length of $2\,D$ is mounted downstream of the main body. The length of the nozzle is selected to obtain an impingement of the shed shear layer just upstream of the end of the nozzle as it is observed in axisymmetric launcher configurations. For the inner shape of the nozzle, a parabolic thrust optimized geometry with a design Mach number of $M_e = 2.6$ at the exit section is chosen. The main body diameter D and the step height $h = 0.3D$ of the BFS are chosen as reference values. The origin of the frame of reference is located at the center of the main body's tail. The x-axis defines the streamwise direction and the y-axis the wall-normal direction.

Since the dynamic loads feature the highest nominal amplitudes during the transonic stage of the flight trajectory[18] , the simulations are performed at a freestream Mach number of $M_\infty = 0.8$. The freestream and nozzle flow conditions are summarized in Tab. 1. They are chosen according to a number of experimental investigations recently performed on the same planar launcher at the Bundeswehr University Munich within the framework of the German Collaborative Research Center Transregio 40.

DOI: 10.13009/EUCASS2017-561

Table 1: Freestream and nozzle flow conditions.

	M	Re_D	U [m/s]	p_0 [Pa]	p [Pa]	T_0 [K]	T [K]
Freestream (∞)	0.8	$0.43 \cdot 10^6$	257	$1.2 \cdot 10^5$	$0.787 \cdot 10^5$	290	257
Nozzle exit (e)	2.59	$1.55 \cdot 10^6$	642	$6 \cdot 10^5$	$0.305 \cdot 10^5$	290	124

2.2 Zonal RANS/LES flow solver

The time-resolved computations are performed using a zonal RANS/LES solver which is based on a finite-volume method. The computational domain is split into several zones, see Fig. 3. In the zones where the flow is attached, i.e., the flow around the forebody and inside the nozzle, the RANS equations are solved. The wake flow characterized by the separated shear layer is determined by the LES.

The Navier-Stokes equations of a three-dimensional unsteady compressible fluid are discretized second-order accurate mixed centered/upwind advective upstream splitting method (AUSM) scheme for the Euler terms. The non-Euler terms are approximated by a second-order accurate centered scheme. For the temporal integration an explicit 5-stage Runge-Kutta method of second-order accuracy is used. The monotone integrated LES (MILES) method determines the impact of the sub-grid scales. The solution of the RANS equations is based on the same discretization method. To close the time-averaged equations the one-equation turbulence model of Fares & Schröder[19] is used. For a comprehensive description of the flow solver see Statnikov et al.[10,20] .

The transition from the RANS to the LES domain is determined by the reformulated synthetic turbulence generation (RSTG) method developed by Roidl et al.[21,22] , which allows to reconstruct the turbulent fluctuations in the LES inlet plane based on the upstream RANS solution. This method generates turbulent fluctuations as a superposition of coherent structures and extends the idea of the synthetic eddy method (SEM) by Jarrin et al.[23] . The turbulent structures are generated at the inlet plane by superimposing virtual eddy cores, which are defined at random positions $\boldsymbol{x}_i$ in a virtual volume V_{virt}. This volume encloses the inlet plane and exhibits the dimension of the turbulent length scale l_x, the boundary-layer thickness at the inlet δ_0, and the width of the computational domain L_z in the streamwise, the wall-normal, and the spanwise direction. To take the inhomogeneity of the turbulent scales in the wall-normal direction into account, the virtual eddy cores are described by different shape factors and length and time scales depending on the wall-normal distance. Having N synthetic eddies, the normalized stochastic velocity fluctuations u'_m at the LES inlet plane are determined by the sum of the contribution $u^i_m(\boldsymbol{x}, t)$ of each eddy core i

$$u'_m(\boldsymbol{x}, t) = \frac{1}{\sqrt{N}} \sum_{i=1}^{N} \underbrace{\epsilon_i f^i_{\sigma,m}(\boldsymbol{x} - \boldsymbol{x}_i)}_{u^i_m(\boldsymbol{x},t)} \tag{1}$$

where ϵ_i is a random number within the interval $[-1, 1]$, $f^i_{\sigma,m}$ is the shape function of the respective eddy, and the subscript m denotes the Cartesian coordinates in the streamwise, the wall-normal, and the spanwise direction. The final velocity components at the LES inflow plane u_m are composed of an averaged velocity component $u_{RANS,m}$ from the RANS solution and the normalized velocity fluctuations u'_m which are subjected to a Cholesky decomposition A_{mn} to assign the values of the target Reynolds-stress tensor $R_{mn} = A^T_{mn} A_{mn}$ corresponding to the turbulent eddy viscosity of the upstream RANS

$$u_m(\boldsymbol{x}, t) = u_{RANS,m} + A_{mn} u'_m(\boldsymbol{x}, t) \ . \tag{2}$$

To enable an upstream information exchange, i.e., a full bidirectional coupling of the LES and RANS zones, the time averaged static pressure of the LES zone is imposed after a transition of three boundary-layer thicknesses at the end of the overlapping zone onto the RANS outflow boundary. The temporal window width used to compute the pressure for the RANS outflow plane is chosen such that high frequency oscillations of the LES pressure field are filtered out. A more detailed description of the zonal RANS/LES method specifying the shape functions and length scales is given in Ref.[21,22] .

Besides the RSTG method, the approach of Batten et al.[24] is used in the center of the nozzle flow at the LES inlet plane to generate random fluctuations exhibiting no specific length and time scales as they occur in boundary layers.

DOI: 10.13009/EUCASS2017-561

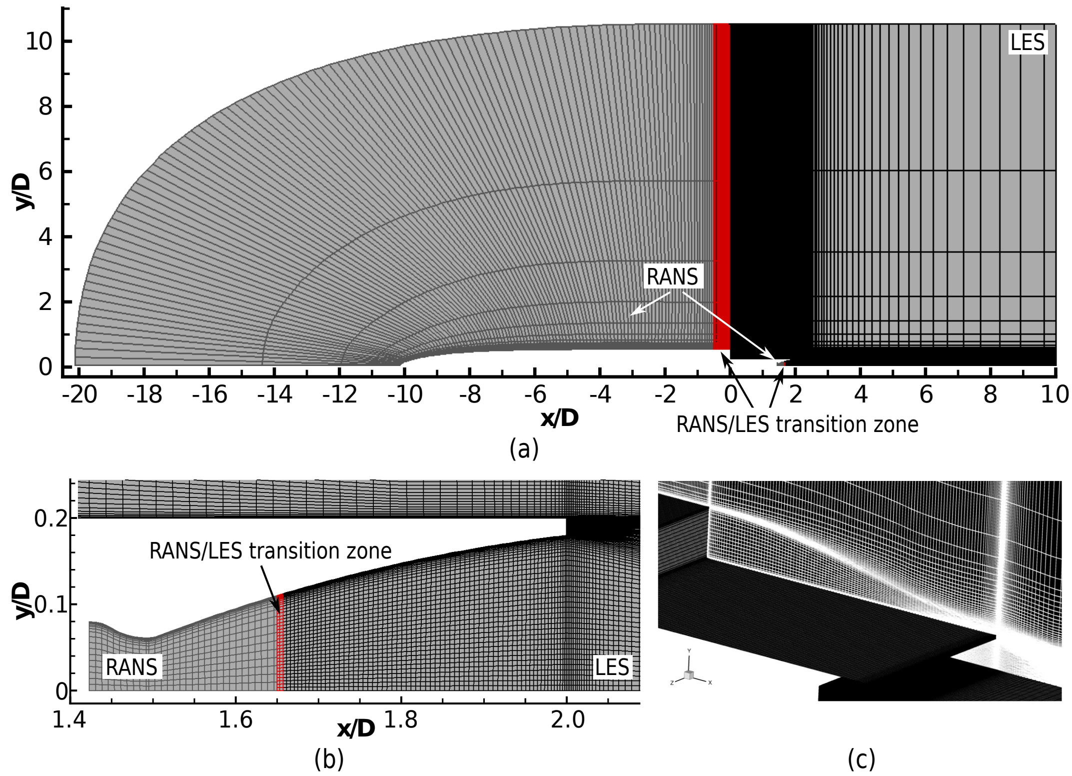

Figure 3: (a) Overview of the zonal grid topology; (b) zonal grid for the nozzle region; (c) LES grid for the wake zone.

2.3 Computational mesh

In the zonal approach, the computational domain is divided into a RANS part enclosing the attached flow around the forebody and inside the nozzle and an LES grid for the wake, as shown in Fig. 3. To reduce the computational costs, the simulation is only performed for the upper half of the flow field, i.e., a symmetry condition is imposed in the $y/D = 0$ plane. The RANS domain around the forebody extends to approximately 10D in the wall-normal direction and ends at $x/D = -0.05$ just upstream of the trailing edge of the main body located at $x/D = 0$. The LES section extends in the streamwise direction from $x/D = -0.5$ to $x/D = 10$ and in the wall-normal direction, like the RANS mesh from $y/D = 0$ to $y/D = 10$. To ensure a fully developed boundary layer a transition length of approximately three boundary-layer thicknesses is required by the RSTG approach. Since the boundary-layer thickness directly upstream of the base shoulder is $\delta = 0.15D$, the LES inflow plane is positioned at $x/D = -0.5$ to guarantee a fully developed turbulent boundary layer upstream of the BFS geometry. The LES inflow plane inside the nozzle is located at $x/D = 1.65$.

The characteristic grid resolution in the area within the transition zone in inner wall units $l^+ = u_\tau/\nu$ is $\Delta x^+ = 50$, $\Delta y^+ = 2$, and $\Delta z^+ = 30$ for the LES zone and $\Delta x^+ = 350$, $\Delta y^+ = 1$, and $\Delta z^+ = 1500$ for the RANS domain. The resolution is chosen according to typical mesh requirements in wall-bounded flows outlined by Choi & Moin[25] . In total 222 million grid points are used for the zonal setup. The number of grid points in each direction for the respective domains are listed in Tab. 2.

2.4 Dynamic mode decomposition

The dynamic mode decomposition (DMD) is a data-driven modal decomposition technique based on the Koopman operator to determine a basis of non-orthogonal spatial modes each associated with a specific constant frequency from a multi-dimensional data field obtained from time-resolved experiments or simulations. The extracted modes can be used to identify characteristic structures like vortices and eddies being of particular importance to the underlying flow field. In addition, the modes can serve as a basis for a reduced-order model, thus the original dynamical system can be projected onto a modeled system with fewer degrees of freedom. In contrast to a model-based approach, a data-driven technique like DMD offers the advantage that no information about the underlying, mostly nonlinear and high-dimensional dynamical system is needed. The DMD algorithm was initially developed by Schmid[26] , including an

DOI: 10.13009/EUCASS2017-561

Table 2: Number of mesh points in each direction for the respective domains

	N_x	N_y	N_z	Summe
RANS (forebody)	481	133	17	$1.09 \cdot 10^6$
RANS (nozzle)	605	191	9	$1.04 \cdot 10^6$
LES (main body)	209	97	801	$16.2 \cdot 10^6$
LES (near wake)	465	193	801	$71.9 \cdot 10^6$
LES (nozzle)	273	157	801	$34.3 \cdot 10^6$
LES (far wake)	263	461	801	$97.1 \cdot 10^6$
Total				$222 \cdot 10^6$

economy-sized singular value decomposition (SVD) to guarantee a more robust calculation in case of an ill-conditioned input dataset. As usual for data-driven techniques, the DMD algorithm requires a sequence of equidistantly sampled snapshots arranged in form of the data matrix $\psi_0 = \{\psi_1, \psi_2, \cdots, \psi_N\}$, where $\psi_n := \psi(x, y, z, t_n)$ represents the high-dimensional flow field at the discrete time step t_n. The DMD algorithm projects the data matrix onto a set of non-orthogonal spatial modes

$$\underbrace{[\psi_0\ \psi_1\ \ldots\ \psi_{N-1}]}_{\psi_0} \approx \underbrace{[\phi_1\ \phi_2\ \cdots\ \phi_N]}_{\Phi} \cdot \underbrace{\begin{pmatrix} a_1 & & & \\ & a_2 & & \\ & & \ddots & \\ & & & a_N \end{pmatrix}}_{D_a = diag\{a\}} \underbrace{\begin{pmatrix} 1 & \mu_1 & \cdots & \mu_1^{N-1} \\ 1 & \mu_2 & \cdots & \mu_2^{N-1} \\ 1 & \vdots & \ddots & \vdots \\ 1 & \mu_N & \cdots & \mu_N^{N-1} \end{pmatrix}}_{V_{and}} . \tag{3}$$

The quantity ϕ_n represents the spatial modes, a_n the amplitude of the corresponding DMD mode, and V_{and} the Vandermonde matrix containing the eigenvalues μ_n, which determine the temporal evolution, i.e., the frequencies and decay rates of the modes. To determine the unknown amplitudes a_n the following convex optimization problem is solved

$$\underbrace{\text{minimize}}_{a} \ ||\psi_0 - \Phi D_a V_{and}||_F^2 . \tag{4}$$

This means that the amplitudes are chosen such that the entire input data sequence is optimally approximated. To reconstruct the temporally developing flow field the entire or a subset of the DMD modes can be superimposed according to the following equation

$$v(x, y, z, t) = \sum_{n=1}^{N} a_n e^{(\lambda_n t)} \phi_n(x, y, z) . \tag{5}$$

The quantity λ_n is the complex frequency which is determined by

$$\lambda_n = \frac{\log(\mu_n)}{\Delta t} = \underbrace{\frac{\log|\mu_n|}{\Delta t}}_{D_n} + i \cdot \underbrace{\arctan\left(\frac{\mu_{n,imag}}{\mu_{n,real}}\right)\frac{1}{\Delta t}}_{\omega_n} , \tag{6}$$

where the real part D_n is the decay rate and the imaginary part ω_n is the angular frequency of the respective mode.

The DMD algorithm is parallelized using MPI and ScaLAPACK to handle the large amount of data, the I/O is performed using the HDF5 parallel file format. For a more detailed description of the DMD algorithm, the reader is referred to Schmid[26] and Jovanovic et al.[27] .

3. Results

The discussion of the results is divided into three parts. First, the general characteristics of the wake flow topology plus jet are described in detail and compared to results of a previously investigated configuration without a thrust nozzle and jet plume thus being similar to a classical BFS flow. Subsequently, the dynamic behavior of the wake flow is investigated by a classical statistical analysis, i.e., Fourier transformation. Finally, a reduced-order approach based on the DMD technique is performed to detect spatio-temporal modes which are responsible for the dominant peaks found in the spectral analysis.

DOI: 10.13009/EUCASS2017-561

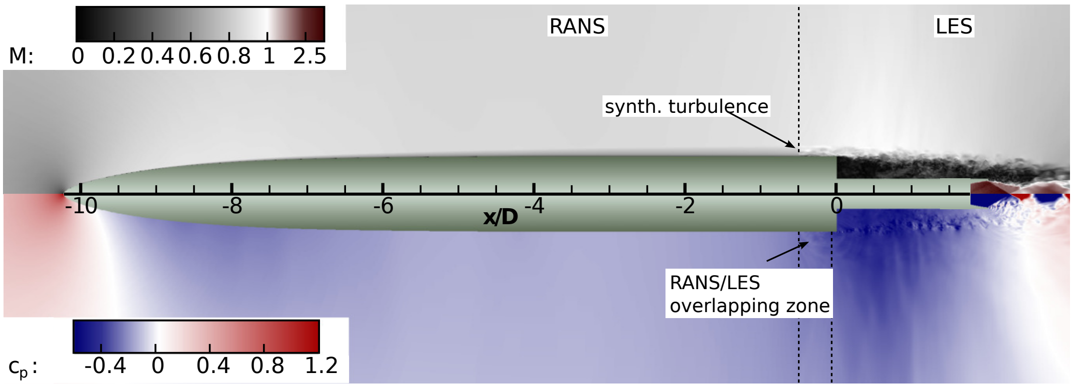

Figure 4: Flow topology of the generic planar space launcher configuration in the center cross-section at $z/D = 0.6$: Instantaneous Mach number distribution (top); pressure coefficient (bottom).

3.1 Characteristics of the wake flow topology

To visualize the overall flow topology around the forebody and the wake, the instantaneous distribution of the Mach number and the pressure coefficient are shown in Fig. 4 for the generic space launcher configuration. Downstream of the stagnation point at the tip of the generic space launcher, the incoming freestream with a Mach number of $M_\infty = 0.8$ continuously accelerates along the fairing to a maximum Mach number of $M \approx 0.91$ around the launcher's nose. Further downstream towards the base shoulder of the main body, the flow decelerates again to $M \approx 0.85$ in the overlapping zone. At the abrupt junction between the main body and the nozzle, the incoming turbulent boundary layer separates and a turbulent free-shear layer emanates.

The development of the shed shear layer is shown in the upper part of Fig. 5(a) by the instantaneous distribution of the spanwise vorticity component in the center cross-section at $z/D = 0.6$. Due to shear layer instabilities, the initially small turbulent structures start to grow similar to structures observed in the planar free-shear layers by Winant & Browand[28] leading to a continuously broadening shear layer as qualitatively evidenced by the turbulent structures illustrated by contours of the Q-criterion in Fig. 5(b). At about the center of the nozzle extension at $z/D = 1$, the initially mainly in the streamwise direction oriented vortices are replaced by three-dimensional structures approaching the nozzle outer surface. Finally, they either impinge on the surface approximately between $1 < x/D < 2$ or pass downstream without interacting with the nozzle surface. In addition, downstream of the overexpanded fully flown nozzle the characteristic pattern consisting of shocks and alternating expansion and compression waves is visible in the instantaneous Mach number and pressure coefficient distribution in Fig. 4. In the mixing region between the jet plume and the outer flow in the upper part of Fig 5(a) intensive turbulent structures are generated due to the strong shear of the mean flow field.

The time averaged flow field is given in the lower part of Fig 5(a). Shown are the time and spanwise averaged streamwise velocity contours and streamlines. At the base shoulder the incoming outer flow expands followed by a

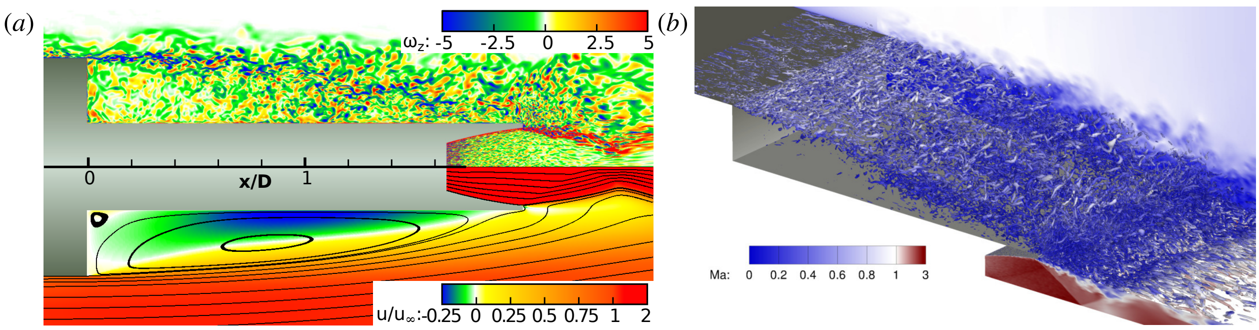

Figure 5: Flow topology: (a) Instantaneous distribution of the spanwise vorticity component in the center cross-section at $z/D = 0.6$ (top); time and spanwise averaged streamwise velocity contours and streamlines (bottom); (b) visualization of the turbulent structures using Q-contours colored by the instantaneous Mach number.

DOI: 10.13009/EUCASS2017-561

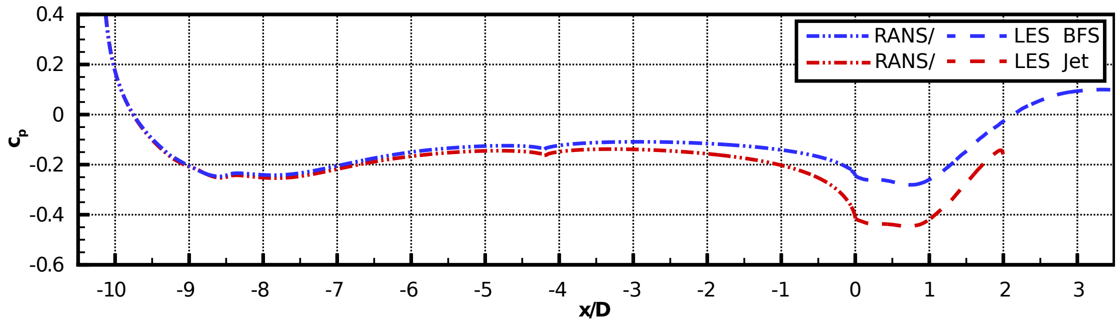

Figure 6: Streamwise distribution of the mean wall-pressure coefficient; comparison of the configuration with and without the propulsion jet.

gradually recompression further downstream when the flow realigns in the streamwise direction as evidenced by the pressure coefficient distribution in the lower part of Fig. 4. Downstream of the base a large recirculation region characterized by a lower pressure level compared to the freestream forms causing the base drag. The maximum backflow velocity found in the center of the recirculation region is $u/u_\infty \approx -0.25$, which is in accordance with the measurements in [3] . The resulting time-averaged reattachment position is $x/D = 1.9$ or $x/h = 6.3$ for the step height $h = 0.3D$. Since the mean reattachment length in the preceding study without the overexpanded jet was $x/h = 7$,[10] the jet decreases the reattachment length slightly. The averaged flow field also exhibits a secondary recirculation region in the corner of the backward facing step which is common in BFS flows[8] .

As mentioned above, the separation at the tail of the main body results in a strong pressure drop at the base resulting in the base drag. To further evaluate the influence of the jet emanating from the nozzle on the pressure distribution along the launcher's surface, the wall-pressure coefficient $c_p = (p - p_\infty)/q_\infty$ with $q_\infty = 0.5\rho_\infty u_\infty^2$ of the fully coupled RANS/LES simulation is shown as a function of the streamwise position for the flow with and without jet in Fig. 6. Due to the local acceleration along the nose, the pressure initially drops to a local minimum of $c_p = -0.25$ and then increases again as the flow decelerates along the forebody. On the first half of the nozzle extension at $0 < x/D < 1$, the pressure coefficient exhibits a plateau-like minimum with a constant value of $c_p = -0.45$, followed by a quasi linear increase near the end of the nozzle which is caused by the impinging shear layer. The low base pressure exhibits a significant upstream influence on the attached boundary layer around the forebody. The flow accelerates already upstream of the shoulder leading to a decreasing pressure coefficient. This is taken into account in the simulation due to the full bidirectional coupling of the zonal method enabling an upstream propagation of the information from the LES to the RANS zone. The comparison between the present jet case with the BFS configuration without jet shows a qualitatively similar development of the pressure coefficient. The absolute pressure level in the recirculation region, however, is decreased in the jet configuration, which is due to the considerably lower pressure level at the nozzle exit and the high streamwise momentum of the overexpanded supersonic jet that accelerates of the outer flow. The low base pressure reduces the wall pressure up to the center of the forebody. This result also shows the necessity of the bidirectional coupling between the LES and the RANS zones. Note that the current findings deviate from the results by Deprés et al.[1] for an axisymmetric case. However, they considered an adapted jet which is why only a slight reduction of the pressure coefficient on the nozzle surface occurred.

The streamwise distribution of the root-mean-squre (rms) coefficient of the pressure fluctuations $c_{prms} = \sqrt{\overline{p'^2}}/q_\infty$ on the nozzle surface is given for both configurations in Fig. 7. The pressure fluctuations of the jet configuration exhibit a small local extremum just downstream of the backward facing step at $x/D = 0.2$ which is caused by the secondary recirculation region. Further downstream at $x/D > 0.5$ the rms value steadily increases in the streamwise direction, reaches its maximum just upstream of the time-averaged reattachment position, and then slightly decreases near the end of the nozzle. The increase in the pressure fluctuations around the mean reattachment position is generated by the vortical structures in the shear layer impinging on the nozzle surface. Note that the streamwise position, where the rms value starts to increase, i.e., at $x/D \approx 0.8$ coincides with the location of the mean pressure recovery in Fig. 6. Compared to the no-jet study, the general development of the pressure fluctuations is quite similar. Only the maximum value at the end of the nozzle extension is slightly increased.

To juxtapose the streamwise evolution of the shear layer and to determine the suction effect of the overexpanded jet, the time averaged profiles of the streamwise velocity component of the two configurations are presented at several positions in the wake in Fig. 9. Besides the aforementioned reduction of the mean reattachment length in the jet configuration, an acceleration of the wake flow is clearly visible due to the jet's suction effect. Even the incoming turbulent boundary layer is accelerated due to the low static pressure in the recirculation region. In addition, the center

DOI: 10.13009/EUCASS2017-561

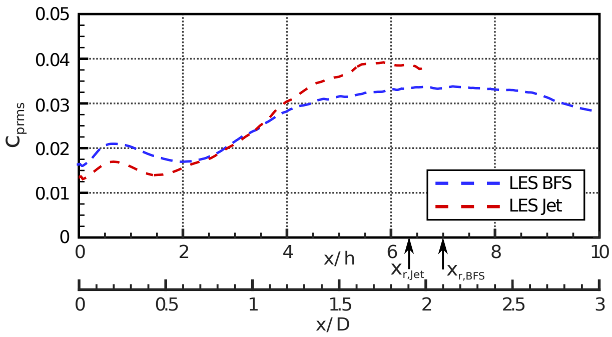

Figure 7: Streamwise distribution of the root-mean-square wall-pressure coefficient, the time averaged reattachment positions are marked by $x_{r,jet}$ and $x_{r,BFS}$.

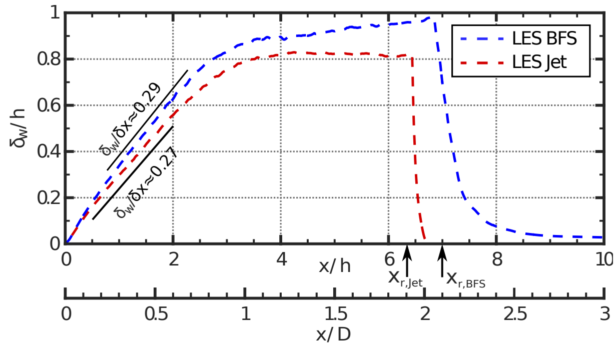

Figure 8: Streamwise development of the vorticity thickness δ_w, the time averaged reattachment positions are marked by $x_{r,jet}$ and $x_{r,BFS}$.

of the shear layer defined as the location where the streamwise velocity gradient in the wall-normal direction is highest, is positioned closer to the nozzle surface for the jet configuration indicating that the shear layer is shed at a larger angle towards to nozzle fairing.

Next, the quantitative development of the characteristic thickness of the shear layer is discussed based on the streamwise evolution of the vorticity thickness defined by Brown & Roshko[29] as

$$\delta_w(x) = \frac{\langle u \rangle_{max}(x) - \langle u \rangle_{min}(x)}{\max\left(\frac{\partial \langle u \rangle(x,y)}{\partial y}\right)\Big|_x} . \tag{7}$$

The quantity $\langle u \rangle(x, y)$ is the time averaged streamwise velocity and the subscripts *max*, *min* denote the maximum and minimum value in the wall-normal direction. The streamwise variation of the vorticity thickness of both configurations is shown in Fig. 8. The overall development of the vorticity thickness can be divided into three major sections. In the range $0 < x/D < 1$ the vorticity thickness of the jet configuration initially grows linearly at a rate of $\partial\delta_w/\partial x = 0.27$. This growth rate is about 50% higher than for classical planar mixing layers. Brown & Roshko[29] report for $U_2 = \langle u \rangle_{min} = 0$ a growth rate of $\partial\delta_w/\partial x = 0.18$. This increase is caused by the recirculation region enhancing the shear due to the backflow which intensifies the turbulent structures in the mixing layer. In the second region, located at the second half of the nozzle extension, where the shear layer is strongly effected by the nozzle restricting its further spreading, the initial linear growth strongly decreases and finally, the vorticity thickness reaches a plateau with $\delta_w \approx 0.8$. This streamwise development process of the shear layer which is characterized by an initial linear growth followed by a plateau region further downstream is in good agreement with the work on BFS flows by Simpson[5] . Further downstream, i.e., near the mean reattachment position, the vorticity distribution abruptly drops by more than

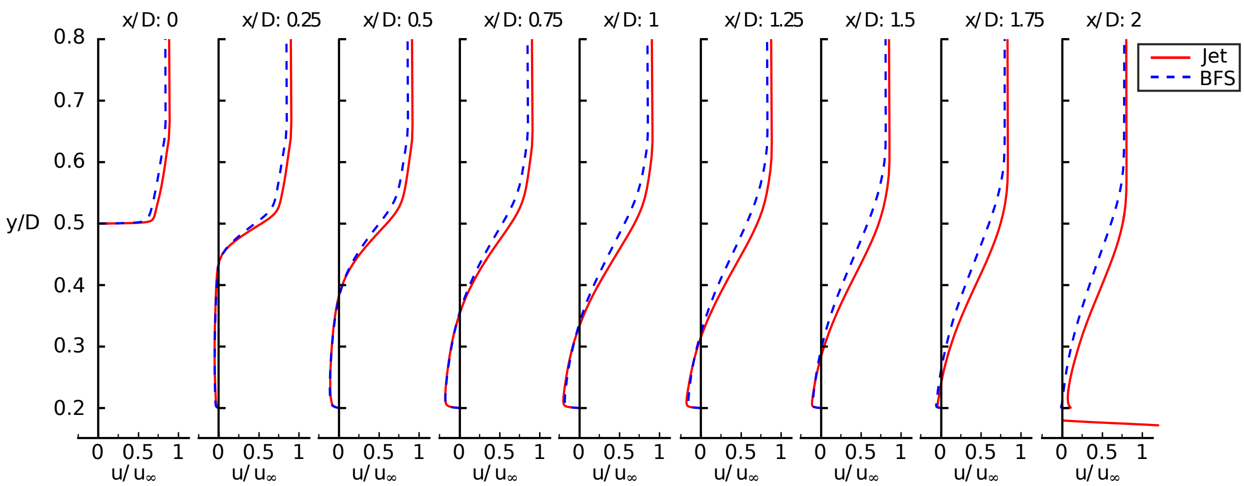

Figure 9: Time and spanwise averaged profiles of the streamwise velocity component in the wake of the jet configuration and the planar jetless BFS configuration.

DOI: 10.13009/EUCASS2017-561

one order of magnitude. This change is caused by the development of a new attached boundary layer. Compared to the configuration without jet the initial growth rate and the maximum vorticity thickness of the jet configuration is slightly decreased. This is caused by the aforementioned larger inclination of the shed shear layer towards the nozzle fairing. Consequently, the abrupt drop of the vorticity thickness, which marks the mean reattachment position of the free-shear layer, is located further upstream.

The Q-criterion contours and the spanwise vorticity distribution in Fig. 5 show that the turbulent wake of the planar space launcher configuration is characterized by the interaction of a large number of structures exhibiting various time and length scales. The strong time dependence of the wake is also evident in the upper illustrations in Fig. 10 showing the instantaneous streamwise velocity distribution and streamlines in the cross-section at $z/D = 0$ at two time instants. At $t = t_0$ the recirculation region is greatly enlarged and the free-shear layer passes over the nozzle without impinging on it. Later at $t + \Delta t$ with $\Delta t = 14 t_{ref}$, where $t_{ref} = D/u_\infty$ is the reference time unit defined as the time a particle moving at freestream velocity u_∞ needs to cover a distance equal the main body's thickness D, the recirculation region has collapsed and the shear layer impinges on the nozzle surface in the range $1.2 < x/D < 1.4$, which is more than $0.5D$ upstream of the time-averaged reattachment position. This oscillation of the recirculation region and consequently the variation of the impingement location is characteristic for the separating-reattaching flow past a BFS flow. Despite the straight separation line defined by the edge at the BFS, the recirculation region and the shear layer exhibit a strong spanwise variation leading to an alteration of the streamwise impingement location depending on the spanwise position. This is illustrated by the instantaneous distribution of the skin-friction coefficient on the nozzle surface in Fig. 10. The skin-friction coefficient distribution exhibits wedge-shaped reattachment regions with a spanwise wavelength of approximately $\lambda/D = 0.6$ which alternate their spanwise position over time. A similar time-dependent behavior was observed in the planar jetless BFS configuration[10,11] . That is, the jet seems to not effect the overall dynamics of the wake flow.

3.2 Temporal spectral analysis of the wake flow dynamics

To evaluate the temporal periodicity of the wake dynamics and the resulting dynamic loads, the power spectral density (PSD) of the wall pressure fluctuations is discussed in the following. The PSD computation is based on a sequence of 2048 time instants equidistantly sampled with $\Delta t = 0.1 D/u_\infty$. Welch's algorithm with Hanning windows of 512 samples each and an overlap of 50% is used. Hence, according to the Nyquist criterion frequencies in the range of $1.95 \cdot 10^{-2} < Sr_D < 5$ can be determined. To improve the statistical quality of the results, the PSD is computed for 401

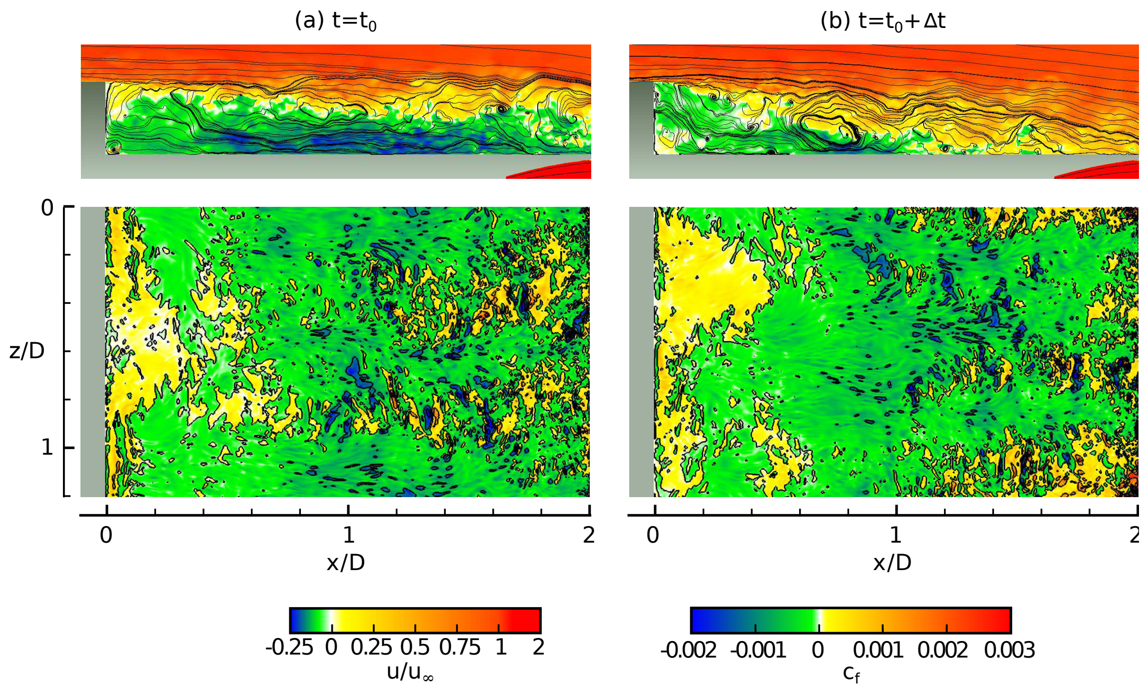

Figure 10: Instantaneous wake flow at two time steps: Streamwise velocity distribution and streamlines in the wake shown in the cross-section at $z/D = 0$ (top); skin-friction coefficient distribution on the nozzle surface.

DOI: 10.13009/EUCASS2017-561

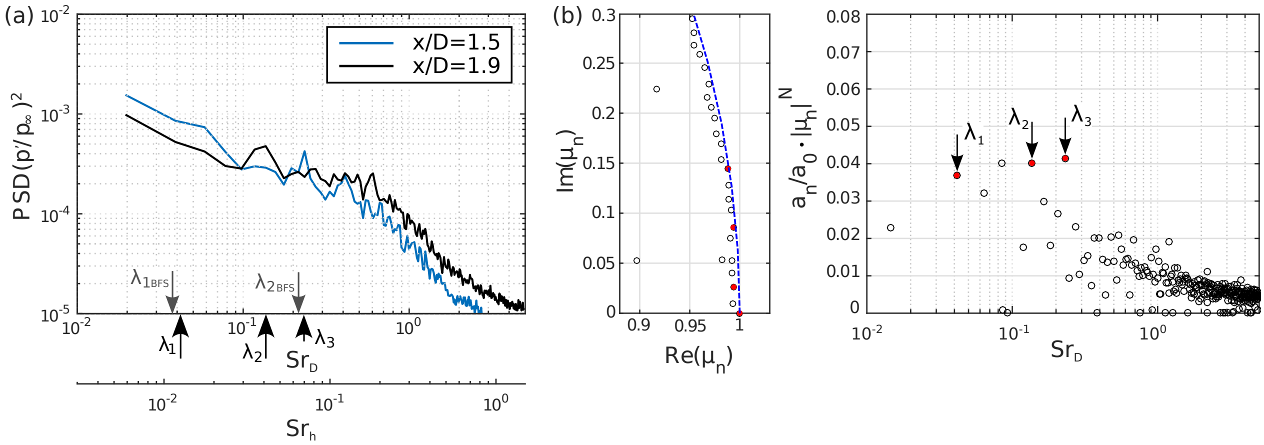

Figure 11: (a) Power spectral density of the wall pressure fluctuations p'/p_∞ at $x/D = 1.5$ and $x/D = 1.9$; (b) normalized DMD spectrum of the three-dimensional velocity and pressure field; eigenvalues $\mu_n = e^{(\lambda_n \Delta t)}$ (left), normalized amplitude distribution versus frequencies $\Im(\lambda_n)$ (right).

points equidistantly distributed in the spanwise direction and subsequently averaged in the frequency space.

The resulting PSD spectra at several streamwise positions near the impingement location of the separated shear layer is given in Fig. 11(a). Note that in addition to the PSD spectrum three frequencies λ_1, λ_2, and λ_3 are marked, which are the basis of the later performed DMD analysis, and two frequencies $\lambda_{1,BFS}$ and $\lambda_{2,BFS}$ denote the frequencies of the previous investigation of the no-jet configuration[10] . The spectra at both positions reveal a flat low frequency characteristic range around a Strouhal number of $Sr_D = 0.04$ ($Sr_h = 0.012$) based on the launchers diameter D or the step hight h and the freestream velocity. This low frequency content was also detected in pure BFS flows and is associated to an enlarging and contracting of the separation bubble[4] . The frequency also coincides with the low frequency mode describing a three-dimensional cross-pumping motion observed in the no-jet BFS configuration[10] . The two spectra show two distinct peaks at $Sr_D = 0.14$ ($Sr_h = 0.042$) and $Sr_D = 0.23$ ($Sr_h = 0.069$). The peak at $Sr_D = 0.23$ matches the high frequency mode of the no-jet BFS configuration[10] which is associated to a cross-flapping motion of the shed shear layer. However, the distinct peak at $Sr_D = 0.14$ in the spectra just upstream of the nozzle lip at $x/D = 1.9$ did not occur in the jetless configuration, i.e., it is caused by the overexpanded jet.

To understand the underlying flow phenomena leading to this periodic behavior, a dynamic mode decomposition is conducted to extract dominant spatio-temporal modes from the time resolved three-dimensional flow field and to reduce the complex flow physics to a few degrees of freedom.

3.3 Modal analysis

The dynamic mode decomposition is performed using $N = 512$ samples of the three-dimensional velocity and pressure field of the wake. The samples are equidistantly distributed with a frequency of $Sr_D = 10$. To save computational costs, the spatial resolution was reduced by using only every second point in the wall normal direction and every fourth point in the spanwise direction. The resulting DMD spectrum is shown in Fig. 11(b). The complex DMD eigenvalues μ_n are plotted together with the unit circle to enable the assessment of the decay rates. The amplitudes a_n of the DMD modes normalized by the amplitude a_{mean} of the mean mode and multiplied by the respective damping $|\mu_n|^N$ are shown as a function of their dimensionless frequency $Sr_D = Im(\lambda_n)/(2\pi\Delta t)$. The multiplication by the damping factor reduces the amplitudes of transient modes which immediately decay and consequently are of minor importance for the overall flow dynamics. The three most stable modes, i.e., $Sr_{D,1}(\lambda_1) = 0.042$, $Sr_{D,2}(\lambda_2) = 0.137$, and $Sr_{D,3}(\lambda_3) = 0.231$, are identified and marked by red dots. The dimensionless frequencies of these modes coincide with the characteristic frequencies of the PSD spectra of the pressure fluctuations shown in Fig. 11(a).

To visualize the three-dimensional shape belonging to the frequency λ_n, the spatial modes ϕ_n are superimposed with the mean mode ϕ_{mean} and reconstructed in time according to Eq. 5. An instantaneous snapshot of the reconstructed streamwise velocity field is given for the low frequency mode at $Sr_{D,1} = 0.042$ in Fig. 12(a). In addition, the shape of the mode is illustrated by means of the streamwise and wall-normal velocity distribution in the center cross-section in Figs. 12(b) and 12(c). The spatial shape of the first DMD mode exhibits a local minimum in the streamwise velocity component and a local maximum in the wall-normal velocity component near the time averaged shear layer location. Superposing the two velocity components results in a movement of the shear layer away from the wall and towards

DOI: 10.13009/EUCASS2017-561

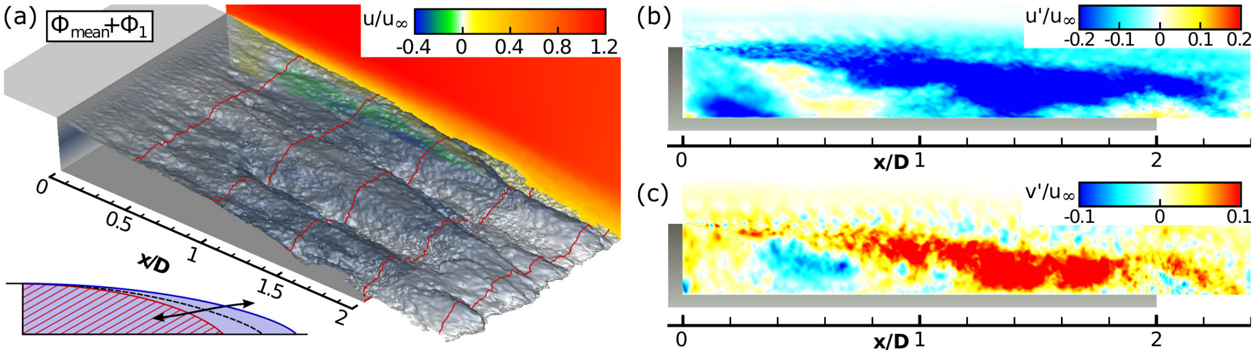

Figure 12: Visualization of the DMD mode ϕ_1: Reconstruction of the wake flow field by superposition of the DMD mode and mean mode (a); streamwise velocity distribution (b); wall-normal velocity distribution (b).

the nozzle lip, i.e., to an enlargement of the separation bubble as schematically illustrated in Fig. 12(a). After one half of the period, the sign of the velocity components changes resulting in a shrinking of the recirculation region. This periodic growing and contracting of the separation bubble was also observed by Schrijer et al.[15] in an axisymmetric configuration and Driver et al.[4] in a 2D-BFS flow and is commonly called shear-layer "flapping". The reconstruction of the full three-dimensional streamwise velocity field reveals that besides the oscillation of the shear layer in the streamwise direction, the reattachment position also strongly alternates in the spanwise direction forming wavy structures. This explains the wedge-shaped reattachment regions observed in the skin-friction distribution. A very similar spatio-temporal mode was found by Statnikov et al.[10] in the no-jet BFS configuration and denoted as "cross-pumping" mode due to the combined longitudinal pumping motion and the strong alteration in the spanwise direction.

The reconstructed flow field and the spatial shape of the second stable DMD mode at $Sr_{D,2} = 0.137$, which is new due to the jet, are presented in Fig. 13. The streamwise and the wall-normal velocity distribution in Figs. 13(b) and 13(c) exhibit two local extrema. At the first extremum at $x/D \approx 0.95$, the streamwise velocity component is negative and the wall-normal velocity component is positive. At the second extremum at $x/D \approx 1.5$, the signs of the velocity components are opposite. The combination of both velocity components leads to an upward and downstream directed shift of the shear layer at the first and an opposite shift at the second extremum. The resulting motion is schematically shown in Fig. 13(a). A half period later, the velocities are reversed leading to an oscillating wavy motion of the shear layer. A comparable undulating motion of the shear layer was detected by proper orthogonal decompostion of the wake flow of an axisymmetric space launcher configuration[15] . The motion is ascribed to large-scale structures inducing momentum injection upstream and momentum ejection downstream of the recirculation region. The instantaneous snapshot of the temporally reconstructed streamwise velocity field shows that like the low frequency mode the second mode has a pronounced three-dimensional shape.

The spatial shape of the third stable mode at $Sr_{D,3} = 0.231$ is similar to the second mode. More precisely, it is characterized by two local extrema in the velocity components leading to a wavelike oscillating motion of the shear layer. The spatial topology of the second and the third stable mode is quite similar to the high frequency "cross-

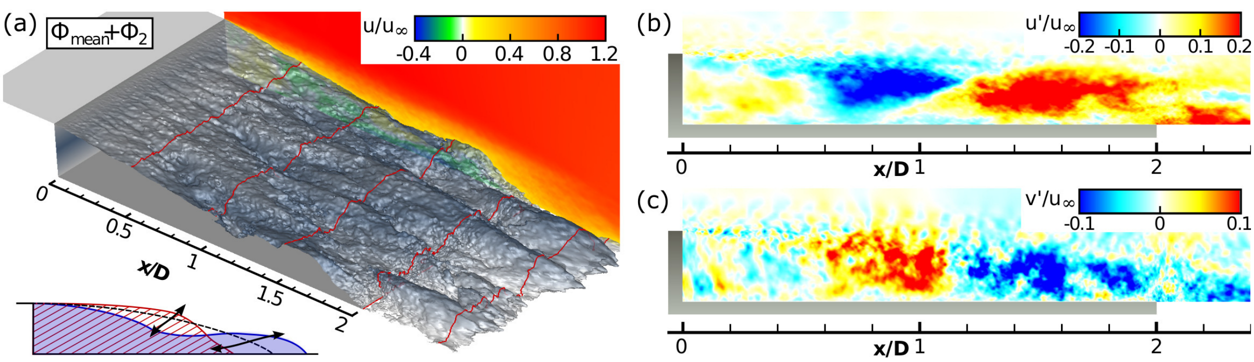

Figure 13: Visualization of the DMD mode ϕ_2: Reconstruction of the wake flow field by superposition of the DMD mode and mean mode (a); streamwise velocity distribution (b); wall-normal velocity distribution (b).

DOI: 10.13009/EUCASS2017-561

flapping" motion at $Sr_D = 0.22$ discovered in the investigation on the pure BFS configuration[10] .

In summary, the DMD analysis yields three stable modes closely matching the frequencies of the PSD of the pressure fluctuations. The low frequency mode at $Sr_{D,1} = 0.042$ and the high frequency mode at $Sr_{D,3} = 0.231$ which describe a periodical growth and collapse of the recirculation bubble and an undulating motion of the shear layer are very similar to the DMD modes of the pure BFS configuration. The second stable mode at a frequency of $Sr_{D,2} = 0.137$ was not found in the BFS flow. The finite length of the nozzle and the overexpanded jet define the formation and shedding of large-scale rotational structures causing the wave-like motion of the shear layer contained in this mode.

4. Conclusion & Outlook

The turbulent wake of a generic planar space launcher with an overexpanded jet is numerically investigated at transonic freestream conditions, i.e., $M_\infty = 0.8$ and $Re_D = 4.3 \cdot 10^5$, to analyze the wake flow modes that describe characteristic flow structures, which dominate the interaction of the flow field and the nozzle and as such are related to the buffeting phenomenon. The results are compared to a previous investigation on a pure, no-jet BFS configuration to determine the influence of the overexpanded jet on the wake flow. The simulations are performed using a zonal RANS/LES approach and the time-resolved flow field data are analyzed using the DMD technique.

The wake flow is characterized by the shear layer separating at the shoulder of the main body and impinging on the nozzle. The reattachment location strongly varies about the time averaged position. Despite the straight separation line defined by the edge at the BFS, the recirculation position exhibits a strong spanwise variation. The skin-friction distribution exhibits wedge-shaped reattachment regions temporally alternating their spanwise position. The unsteady behavior of the shear layer and the recirculation region leads to periodic wall pressure fluctuations. Compared to the no-jet configuration, the time averaged reattachment length and the pressure on the nozzle are decreased due to the suction effect of the jet. The influence of the overexpanded jet is apparent far upstream on the main body.

Using a temporal Fourier transform of the wall pressure fluctuations on the nozzle a low frequency characteristic range around $Sr_D = 0.04$ and two distinct peaks at $Sr_D = 0.14$ and $Sr_D = 0.23$ are detected. The underlying fluid motion is identified by dynamic mode decomposition of the three-dimensional velocity and pressure field. Three DMD modes at $Sr_{D,1} = 0.042$, $Sr_{D,2} = 0.137$, and $Sr_{D,3} = 0.231$ which closely match the characteristic frequencies of the pressure spectra are extracted. The analysis of the shape of the first low frequency mode reveals a periodically growing and contracting separation bubble in the streamwise direction. The full three-dimensional reconstruction shows that besides the streamwise variation, the first DMD mode exhibits a pronounced three-dimensionality leading to a formation of wave-like structures explaining the wedge-shaped reattachment regions in the skin-friction coefficient distribution. The second and third mode describe an oscillating wavy motion of the shear layer caused by large-scale rotational structures inducing momentum injection upstream and momentum ejection downstream of the recirculation region. The spatial shape and the characteristic frequency of the first and third DMD mode closely coincide with the "cross-pumping" and "cross-flapping" motion of the pure BFS configuration. However, the second mode at $Sr_{D,2} = 0.137$ was not found in the previous no-jet BFS configuration, indicating that the finite length of the nozzle and the overexpanded jet support the development of the large-scale rotational structures.

Future investigations will focus on the integration of advanced propulsion concepts such as the dual-bell nozzle for the design of efficient next generation space launchers. Particular attention will be paid to a possible coupling between the outer and inner separation during sea-level conditions leading to additional dynamic forces.

5. Acknowledgments

Financial support has been provided by the German Research Foundation (Deutsche Forschungsgemeinschaft – DFG) in the framework of the Sonderforschungsbereich Transregio 40. The authors are grateful for the computing resources provided by the High Performance Computing Center Stuttgart (HLRS) and the Jülich Supercomputing Center (JSC) within a Large-Scale Project of the Gauss Center for Supercomputing (GCS)

References

[1] D. Deprés, P. Reijasse, and J. P. Dussauge, "Analysis of unsteadiness in afterbody transonic flows," *AIAA J.*, vol. 42, no. 12, pp. 2541–2550, 2004.

[2] P. Bradshaw and F. Wong, "The reattachment and relaxation of a turbulent shear layer," *J. Fluid Mech.*, vol. 52, no. 1, pp. 113–135, 1972.

DOI: 10.13009/EUCASS2017-561

[3] J. K. Eaton and J. P. Johnston, "A review of research on subsonic turbulent flow reattachment," *AIAA J.*, vol. 19, no. 9, pp. 1093–1100, 1981.

[4] D. M. Driver, H. L. Seegmiller, and J. G. Marvin, "Time-dependent behavior of a reattaching shear layer," *AIAA J.*, vol. 25, no. 7, pp. 914–919, 1987.

[5] R. L. Simpson, "Turbulent boundary-layer separation," *Ann. Rev. Fluid Mech.*, vol. 21, pp. 205–2034, 1989.

[6] R. Friedrich and M. Arnal, "Analysing turbulent backward-facing step flow with the low-pass-filtered Navier-Stokes Equations," *Journal of Wind Engineering and Industrial Aerodynamics*, vol. 35, pp. 101–128, 1990.

[7] A. Silveria Neto, D. Grand, O. Metais, and M. Lesieur, "A numerical investigation of the coherent vortices in turbulence behind a backward-facing step," *J. Fluid Mech.*, vol. 256, pp. 1–25, 1993.

[8] H. Le, P. Moin, and J. Kim, "Direct numerical simulation of turbulent flow over a backward-facing step," *J. Fluid Mech.*, vol. 330, pp. 349–374, 1997.

[9] I. Lee and H. J. Sung, "Characteristics of wall pressure fluctuations in separated and reattaching flows over a backward-facing step: Part I. Time-mean statistics and cross-spectral analyses," *Experiments in Fluids*, vol. 30, pp. 262–272, 2001.

[10] V. Statnikov, I. Bolgar, S. Scharnowski, M. Meinke, C. J. Kähler, and W. Schröder, "Analysis of characteristic wake flow modes on a generic transonic backward-facing step configuration," *Europ. J. Mech. B/Fluids*, vol. 59, pp. 124–134, 2016.

[11] S. Scharnowski, I. Bolgar, and C. J. Kähler, "Characterization of turbulent structures in a transonic backward-facing step flow," *Flow, Turbulence and Combustion*, pp. 1–21, 2016.

[12] S. Deck and P. Thorigny, "Unsteadiness of an axisymmetric separating-reattaching flow: Numerical investigation," *Physics of Fluids*, vol. 19, no. 065103, 2007.

[13] S. D. R. Pain, P. E. Weiss, "Zonal detached eddy simulation of the flow around a simplified launcher afterbody," *AIAA J.*, vol. 52, no. 9, 2014.

[14] S. Marie, P. Druault, H. Lambare, and F. Schrijer, "Experimental analysis of the pressure-velocity correlations of external unsteady flow over rocket launchers," *Aerospace Science and Technology*, vol. 30, pp. 83–93, 2013.

[15] F. Schrijer, A. Sciacchitano, and F. Scarano, "Spatio-temporal and modal analysis of unsteady fluctuations in a high-subsonic base flow," *Physics of Fluids*, vol. 26, no. 086101, 2014.

[16] V. Statnikov, M. Meinke, and W. Schröder, "Analysis of spatio-temporal wake modes of space launchers at transonic flow," *AIAA Paper*, vol. 2016-1116, 2016.

[17] V. Statnikov, M. Meinke, and W. Schröder, "Reduced-order analysis of buffet flow of space launchers," *J. Fluid Mech.*, vol. 815, pp. 1–25, 2017.

[18] S. David and S. Radulovic, "Prediction of buffet loads on the Ariane 5 afterbody.," *6th International Symposium on Launcher Technologies, Munich, Germany, 8-11 November*, 2005.

[19] E. Fares and W. Schröder, "A general one-equation turbulence model for free shear and wall-bounded flows," *Flow Turbul. Combust.*, vol. 73, pp. 187–215, 2004.

[20] V. Statnikov, T. Sayadi, M. Meinke, P. Schmid, and W. Schröder, "Analysis of pressure perturbation sources on a generic space launcher after-body in supersonic flow using zonal turbulence modeling and dynamic mode decomposition," *Physics of Fluids*, vol. 27, no. 016103, 2015.

[21] B. Roidl, M. Meinke, and W. Schröder, "A reformulated synthetic turbulence generation method for a zonal RANS-LES method and its application to zero-pressure gradient boundary layers," *Int. J. Heat Fluid Flow*, vol. 44, pp. 28–40, 2013.

[22] B. Roidl, M. Meinke, and W. Schröder, "Boundary layers affected by different pressure gradients investigated computationally by a zonal RANS-LES method," *Int. J. Heat Fluid Flow*, vol. 45, pp. 1–13, 2014.

[23] N. Jarrin, S. Benhamadouche, D. Laurence, and R. Prosser, "A synthetic-eddy-method for generating inflow conditions for large-eddy simulations," *Int. J. Heat Fluid Flow*, vol. 27, pp. 585–593, 2006.

DOI: 10.13009/EUCASS2017-561

[24] P. Batten, U. Goldberg, and S. Chakravathy, "Interfacing statistical turbulence closures with large-eddy simulation," *AIAA J.*, vol. 42, no. 3, 2004.

[25] H. Choi and P. Moin, "Grid-point requirements for large eddy simulation: Champan's estimates revisited," *Physics of Fluids*, vol. 24, no. 011702, 2012.

[26] P. J. Schmid, "Dynamic mode decomposition of numerical and experimental data," *J. Fluid Mech.*, vol. 656, pp. 5–28, 2010.

[27] M. R. Jovanovic, P. J. Schmid, and J. W. Nichols, "Sparsity-promoting dynamic mode decomposition," *Physics of Fluids*, vol. 26, no. 024103, 2014.

[28] C. D. Winant and F. K. Browand, "Vortex pairing: The mechanism of turbulent mixing-layer growth at moderate reynolds number," *J. Fluid Mech.*, vol. 63, no. 2, pp. 237–255, 1974.

[29] G. L. Brown and A. Roshko, "On density effects and large structure in turbulent mixing layer," *J. Fluid Mech.*, vol. 64, no. 4, pp. 775–816, 1974.